Computers and Concrete, *Vol. 15, No. 1 (2015) 103-126*
DOI: http://dx.doi.org/10.12989/cac.2015.15.1.103

An improved 1D-model for computing the thermal behaviour of concrete dams during operation. Comparison with other approaches

D. Santillán[*a], E. Salete[b], M.Á. Toledo[b] and A. Granados[a]

Technical University of Madrid, Department of Civil Engineering: Hydraulic and Energy Engineering C/Profesor Aranguren s/n, 28040 Madrid, Spain

(Receive June 10, 2014, Revised November 1, 2014, Accepted November 3, 2014)

Abstract. Thermal effects are significant loads for assessing concrete dam behaviour during operation. A new methodology to estimate thermal loads on concrete dams taking into account processes which were previously unconsidered, such as: the evaporative cooling, the night radiating cooling or the shades, has been recently reported. The application of this novel approach in combination with a three-dimensional finite element method to solve the heat diffusion equation led to a precise characterization of the thermal field inside the dam. However, that approach may be computationally expensive. This paper proposes the use of a new one-dimensional model based on an explicit finite difference scheme which is improved by means of the reported methodology for computing the heat fluxes through the dam faces.
The improved model has been applied to a case study where observations from 21 concrete thermometers and data of climatic variables were available. The results are compared with those from: (a) the original one-dimensional finite difference model, (b) the Stucky-Derron classical one-dimensional analytical solution, and (c) a three-dimensional finite element method. The results of the improved model match well with the observed temperatures, in addition they are similar to those obtained with (c) except in the vicinity of the abutments, although this later is a considerably more complex methodology. The improved model have a better performance than the models (a) and (b), whose results present larger error and bias when compared with the recorded data.

Keywords: thermal analysis; arch dam; finite element method; finite difference scheme

1. Introduction

Thermal loads are of special interest in some civil infrastructures, such as bridges (Kim *et al.* 2009), prestressed concrete pavements (Nejad *et al.* 2013) or dams (Malm and Ansell 2011). These loads cause the second most major repairs in dams during operation (Douglas 2002). Moreover, they play a vital role in the monitoring tasks of dams (Mata 2011, Mata *et al.* 2013). Concrete temperature varies due to the heat exchange between the structure and the environment. The exchange is caused by the convection phenomenon, the long wave radiation exchange, the solar energy, and the evaporative cooling. Furthermore, the night radiative cooling should be considered when computing the long wave radiation exchange. Heat flows inside the structure due to the

∗Corresponding author, E-mail: david.santillan@upm.es
[a]Lecturer
[b]Professor

http://www.techno-press.org/?journal=cac&subpage=8 ISSN: 1598-8198 (Print), 1598-818X (Online)

conduction mechanism, which is modeled by the heat diffusion equation (Incropera *et al.* 2011).

Solar radiation requires a special treatment since it is not uniformly distributed neither temporally nor spatially across the arch dam faces due to the variable solar incident angle, the curvature of the faces and the shading (Jin *et al.* 2010). The variable position of the sun along the day makes the shadow areas and the incident angle of sunrays change with time.

Models for computing the thermal field of concrete dams during operation can be analytical or numerical. Boundary conditions in numerical models are of imposed heat flux or temperature. Imposed heat flux is adopted in areas above water. Imposed temperature is used in areas below water, where the temperature of boundary nodes is assumed to be equal to water temperature (Léger *et al.* 1993a, Agullo *et al.* 1996, Jin *et al.* 2010, Sheibany and Ghaemian 2006) .

One of the first one-dimensional (1D) analytical solution was proposed by Stucky and Derron (1957). Temperatures of dam faces were assumed to be sinusoidal signals in phase. Later, the solution was extended to periodic but non-harmonic temperatures in the faces with a frequency domain approach (Léger and Leclerc 2007).

A 1D numerical model solved by an explicit finite difference scheme (FDS) was proposed by Agullo *et al.* (1996). The model was successfully applied to arch and gravity dams. Neither shading nor evaporative cooling nor night radiative cooling were considered.

Léger *et al.* (1993a, 1993b) computed the thermal field in a gravity dam by a 2D model solved by the finite element method (FEM). The model did not take into account shading, evaporative cooling and radiative cooling either.

Sheibany and Ghaemian (2006) determined the thermal field of the Karaj double arch dam (Iraq) with a 3D-FEM model. The foundation was not considered since heat exchange between the structure and the rock was neglected. Jin *et al.* (2010) proposed a methodology for computing the temperature on the exposed faces of arch dams with a 3D-FEM model. The model was validated with a case study. Bayaggob *et al.* (2010) developed a 3D finite element code for the coupled thermo-mechanical analysis of roller compacted concrete arch dams. Solar radiation was accounted for by an increase in ambient temperature of 1.0 ºK. Neither evaporative nor night radiative cooling effects were considered in the three previous works.

Thermal studies have been conducted in other civil infrastructures during service. As for instance, 1D models have been developed to calculate the surface temperature and time of wetness and freezing of concrete pavements and bridge decks (Bentz 2000). Models have also been used for predicting the thermal behavior of concrete at early ages. Wojcik *et al.* (2003) developed a model for computing the temperatures and moisture of curing concrete bridge decks. Faria *et al.* (2006) proposed a methodology for analyzing the thermo-mechanical behavior of concrete at early ages. Abdulrazeg *et al.* (2013) modeled the combined thermo-mechanical behavior of roller compacted concrete dams at early ages. A 3D model which accounts for ageing, creep, hydration, construction process and temperature effects on concrete properties was developed. The methodology was applied to the Karun III Arch dam located in Iran (Abdulrazeg *et al.* 2014).

In this paper, the Agullo *et al.* 1D-FDS model is improved by the use of a new methodology proposed by Santillán *et al.* (2014) for computing heat fluxes. The approach accounts for the evaporative cooling, the night radiative cooling, and shading. The concrete temperatures, measured at the thermometers of a case study, are computed through the improved 1D-FDS model and the original 1D-FDS model of Agullo *et al.* Additionally, temperatures are also computed with a 3D-FEM model and the classical analytical solution of Stucky and Derron (1957). Results of the improved methodology are compared with the observed temperatures and also with the estimates of other models, in order to assess its performance. Finally, attributions which explain the similarity of the results of the improved 1D-FDS and the 3D-FEM models are sought.

2. Methodology: thermal models bases and formulations

Heat transfer through a solid body is modeled by the heat diffusion equation, which is expressed in Cartesian coordinates in a continuum isotropic medium with no energy generation and constant properties as (Incropera *et al.* 2011)

$$\frac{\lambda}{\rho c}\left(\frac{\partial^2\theta}{\partial x^2}+\frac{\partial^2\theta}{\partial y^2}+\frac{\partial^2\theta}{\partial z^2}\right)=\frac{\partial\theta}{\partial t} \tag{1}$$

being t the time, θ the temperature, λ the thermal conductivity, ρ the density and c the specific heat. Since the temperature of materials diverges in a narrow range, properties are assumed to be invariant (Léger *et al.* 1993a, 1993b). Boundary conditions are of imposed temperature at points in contact with water and of imposed heat flux in points in contact with air.

2.1 The boundary conditions

2.1.1 Water temperature

The water temperature $\theta_{w,t}$ was computed by the Bofang model (Bofang 1997), given by

$$\begin{aligned}\theta_{w,t}(z,t)=&\left(\frac{\overline{\theta_{w,b}}-\overline{\theta_{w,s}}e^{-0.04H}}{1-e^{-0.04H}}\right)+\left(\overline{\theta_{w,s}}-\frac{\overline{\theta_{w,b}}-\overline{\theta_{w,s}}e^{-0.04H}}{1-e^{-0.04H}}\right)e^{-0.04H}\\&+A_{w,s}e^{-0.018z}\,cos\left(\omega_w(d-d_o-2.15+1.30e^{-0.085z})\right)\end{aligned} \tag{2}$$

where d is the day of the year, z is the water level, $\overline{\theta_{w,b}}$ and $\overline{\theta_{w,s}}$ are respectively the mean annual water temperature at the bottom and the surface of the reservoir, H is the depth of reservoir, $A_{w,s}$ is the annual water temperature amplitude at the surface, ω_w is the angular frequency of the water temperature cycle ($2\pi/365$ days-1) and d_o is the day when the air temperature is maximum.

2.1.2 Heat fluxes

Heat flux $q_{\theta,i,t}$ across node I at time t and concrete temperature θ is the sum of the energy due to convection between dam faces and the air $q_{c,\theta,i,t}$, long wave radiation exchange $q_{r,\theta,i,t}$, evaporative cooling $q_{ev,i,t}$, and solar energy $q_{s,i,t}$ received by node i.

$$q_{\theta,i,t}=q_{c,\theta,i,t}+q_{r,\theta,i,t}+q_{ev,i,t}+q_{s,i,t} \tag{3}$$

q_c was computed by the Newton cooling law, given by Eq.(4),

$$q_{c,\theta,i,t}=h_{i,t}(\theta_{a,i,t}-\theta_{i,t}) \tag{4}$$

in which $h_{i,t}$ is the convection coefficient on node i at time t, $\theta_{a,i,t}$ is the air temperature on node i at time t and $\theta_{i,t}$ is the temperature of the face on node i at time t. $h_{i,t}$ was computed by the Khelbeck formulation, Eq.(5), where $h_{i,t}$ is given in Wm-2ºK-1 and $V_{w,i,t}$ is the wind speed on node i at time t in m/s. The formulation has been applied to concrete box girder bridges (Mirambell and Aguado 1990) and dams (Agullo *et al.* 1996) with accurate results.

$$h_{i,t}=3.67+3.83\,V_{w,i,t} \tag{5}$$

$q_{r,t}$ was computed by the Stefan-Boltzmann law, Eq.(6), where e is the emissivity of the

concrete surface, C_s is the Stefan-Boltzmann constant and $\theta_{sk,t}$ is the temperature of the sky.

$$q_{\theta,r,t} = eC_s({\theta_{sk,t}}^4 - {\theta_t}^4) \tag{6}$$

$\theta_{sk,t}$ can be considered to be equal to the ambient temperature during the day. However, during the night it is lower than θ_a and the night radiative cooling appears. Chen *et al.* (1995) proposed Eq.(7) for computing θ_{sk} as a function of the dew point temperature θ_{dp} which was assessed by the Clausius-Clapeyron equation. The equation depends on the relative humidity and the ambient temperature.

$$\theta_{sk} = \left(0.736 + 0.00577 \cdot \theta_{dp}\right)^{0.25}\theta_a \tag{7}$$

$q_{ev,i,t}$ is a heat loss due to rainfall evaporation on node *i* of the dam face at time *t*. It was given by Eq.(8) as a function of the moisture evaporative flux $q_{m,i,t}$ and the latent heat of evaporative water h_w.

$$q_{ev,i,t} = q_{m,i,t}h_w \tag{8}$$

$q_{m,i,t}$ was given by Eq.(9) in kgs-1, where $E_{s,i,t}$ is the moisture emissivity coefficient in Kgm-2s-1Pa-1, e_s is the saturation vapour pressure in Pa and H_r is the relative humidity.

$$q_{m,i,t} = E_{s,i,t}e_s(1 - H_r) \tag{9}$$

$E_{s,i,t}$ was defined by the Lewis' relationship, given by (Chuntranuluck *et al.* 1998)

$$\frac{h_{i,t}}{E_{s,i,t}} \approx \frac{29c_sP}{18} \tag{10}$$

where c_s is the specific heat capacity of air (1007 JKg-1K-1) and *P* is the total air pressure in Pa.

$q_{s,i,t}$ was given by Eq.(11), where *a* is the solar absorptivity of the concrete and $I_{T,G,i,t}$ is the hourly solar global insolation on the node *i* at time t.

$$q_{s,i,t} = aI_{T,G,i,t} \tag{11}$$

The magnitude of the insolation, the incident angle of the solar rays and shading vary along the day.

The mean hourly global solar insolation on a horizontal surface, I_G, was estimated by the Gueymard model (Gueymard 2000). For other sites of interest, several works provide comparisons between the performance of different models for estimating I_G by using data from different locations in the world, as from the UK (Tham *et al.* 2010), India (Jamil Ahmad and Tiwari 2008) or worldwide (Gueymard 2000). The above mentioned works concluded that the Gueymard model generally gives the best estimations. The ratio r_t between I_G and the daily global insolation H_G for the middle point on each hourly period is provided as a function of the extraterrestrial hourly/daily insolation ratio r_o corrected form the atmospheric effects by the empirical expressions a_1 and a_2, Eq.(12).

$$r_o = \frac{I_{G,o}}{H_{G,o}} = \frac{\pi}{24}\left[\frac{cos\,\omega - cos\,\omega_o}{sin\,\omega_o - \omega_o\,cos\,\omega_o}\right] \tag{12}$$

$$r_t = r_o \left[\frac{1 + cos\,\phi\, cos\,\delta \left(\frac{a_1}{a_2}\right)(cos\,\omega - cos\,\omega_o)}{1 + cos\,\phi\, cos\,\delta \left(\frac{a_1}{a_2}\right) \frac{\omega_o(0.5 + cos^2\,\omega_o) - 0.75\,sin\,2\omega_o}{sin\,\omega_o - \omega_o\,cos\,\omega_o}} \right] \tag{13}$$

$$\begin{aligned} a_1 &= 0.41341K_t + 0.61197K_t^2 - 0.01886K_tS_o + 0.00759S_o \\ a_2 &= Max(0.054, 0.28116 + 2.2475K_t - 1.76118K_t^2 \\ &\quad - 1.84535\,sin\,\alpha_o + 1.6811\,sin^2\,\alpha_o) \end{aligned} \tag{14}$$

in which ϕ is the latitude, δ is the solar declination, ω is the solar hour angle, ω_o is the sunrise hour angle, α_o is daily-average solar elevation outside of the atmosphere and K_t is the clearness index. K_t is the ratio of H_G to the extraterrestrial daily global irradiance on a horizontal surface, $H_{G,o}$. The coefficients were determined with data from 135 radiation stations around the world.

The beam I_b and diffuse I_d hourly components were provided by the CLIMED2 model (De Miguel *et al.* 2001), which is specially suitable for the North Mediterranean belt area. For other sites, several models have been developed such as the Oliveira *et al.* model (Oliveira *et al.* 2002) or Soares *et al.* model for Brazil (Soares *et al.* 2004) or the Lui and Jordan model which was calibrated with data from US and Canada (Duffie and Beckman 2013). Others works have investigated what model is the most suitable for a site, as for instance for Egypt (Elminir 2007) or Cyprus (Jacovides *et al.* 2006).

The CLIMED2 model provides the hourly diffuse fraction k_d as a function of the hourly global clearness index k_t, Eq.(15). k_d is the ratio I_d/I_G and k_t is the ratio $I_G/I_{G,o}$.

$$\begin{aligned} k_d &= 0.995 - 0.081k_t \quad for\ k_t \leq 0.21 \\ k_d &= 0.724 + 2.738k_t - 8.320k_t^2 + 4.967k_t^3 \quad for\ 0.21 < k_t \leq 0.76 \\ k_d &= 0.180 \quad for\ k_t > 0.76 \end{aligned} \tag{15}$$

Shading on the point of interest at the central interval of every hour was computed by a ray-tracing algorithm. A straight line having the sunbeams direction and that passes through the point was traced. If the line did not intersect any object, the point was subjected to sunbeams, otherwise on shadow.

Finally, $I_{T,G,i,t}$ was computed by the Reindl model (Reindl *et al.* 1990), which provides accurate estimations in Spain (Diez-Mediavilla *et al.* 2005). A wide number of works provide information about the most suitable models for other locations, as for instance Noorian *et al.* (2008) in Iran, Vartiainen (2000) in Finland or Notton *et al.* (2006) in France. $I_{T,G}$ is the sum of three components: the beam $I_{T,b}$, the diffuse $I_{T,d}$ and the reflected radiation from the ground $I_{T,r}$. $I_{T,d}$ is composed of the circumsolar $I_{T,d,cs}$, the isotropic $I_{T,d,iso}$ and the horizon brightening $I_{T,d,hb}$ components, Eq. (16-17).

$$I_{T,G} = I_{T,b} + I_{T,d,cs} + I_{T,d,iso} + I_{T,d,hb} + I_{T,r} \tag{16}$$

$$\begin{aligned} I_{T,G} = I_bR_b + I_dAR_b &+ I_d(1-A)\left(\frac{1+cos\,\beta}{2}\right) \\ &+ I_d(1-A)\left(\frac{1+cos\,\beta}{2}\right)\left(\sqrt{\frac{I_b}{I_G}}sin^3\frac{\beta}{2}\right) + I_Gg_r\left(\frac{1-cos\,\beta}{2}\right) \end{aligned} \tag{17}$$

R_b is the ratio of beam insolation on the tilted surface to that on a horizontal surface, β is the slope of the dam face in the point of interest, A is the anisotropy index -Eq.(18)- and g_r is the ground reflectivity.

$$A = \frac{I_b}{I_{G,o}} \tag{18}$$

V_w, θ_a, H_r, rainfall and total air pressure were recorded daily at the weather station of the dam, which led to a corresponding daily determination of q_c, q_r and q_{ev}. Since observations were taken at the weather station, these fluxes were assumed to be spatially uniformly distributed across the dam faces and they were assessed within the concrete temperature range 200-400 ºK every 10 ºK. However, $q_{s,i,t}$ was computed hourly. The ground reflectivity was assumed to be 0.250 in the downstream face (wooded area) and 0.125 in the upstream face (water surface) (Duffie and Beckman 2013).

2.2 The thermal models of concrete dams

2.2.1 The 1D-FDS model

The integration domain was a straight line normal to the mid dam surface and was discretized with a Δx size mesh. Temperature at the node i at time $t+\Delta t$, $\theta_{i,\Delta t}$, was computed by Eq.(19) (Agullo *et al.* 1996).

$$\theta_{i,\Delta t} = \theta_i + \frac{\lambda \Delta t}{\rho c (\Delta x)^2}(\theta_{i+1} - 2\theta_i + \theta_{i-1}) \tag{19}$$

Boundary condition of imposed temperature was considered in nodes that are in contact with water, and of heat flux in nodes in contact with air. Imposed temperature at exterior node i, $\theta_{i,t}$, was expressed by Eq.(20), where $\theta_{w,t}$ is the water temperature

$$\theta_{i,t} = \theta_{w,t} \tag{20}$$

and imposed heat flux was established by the energy balance, Eq. (21),

$$\lambda \frac{\theta_{i+1} - \theta_i}{\Delta x} + q_\theta = \rho c \frac{\Delta x}{2}\left(\frac{\theta_{i,\Delta t} - \theta_i}{\Delta t}\right) \tag{21}$$

where q_θ is the heat flux at time t and concrete temperature θ. Nodes with air properties were considered inside the galleries.

Heat fluxes were computed with the methodology proposed by Agullo *et al.* (1996) and with the one proposed by Santillán *et al.* (2014). The models were denoted as: "Agullo *et al.* 1D-FDS model" and "improved 1D-FDS model".

The domains were discretized with a 0.05 m 1D-mesh size. Initially, a uniform temperature equal to 282.00 ºK was specified and the thermal loads of one year were used for computing the initial thermal field. Loads were applied several times until the solution converged.

2.2.2 The 3D numerical model

The considered domain contained the dam and a finite region of its foundation. Boundary conditions were of the same type as in the 1D-FDS model and were computed with the same methodology. The dam faces were discretized into a finite number of surfaces where solar radiation heat fluxes were computed hourly.

The discretized Eq.(1) at time t yields to the system of equations

$$[C]\{\dot{\theta}_t\} + [K]\{\theta_t\} = \{F\} \tag{22}$$

where [C] is the specific heat matrix, [K] is the conductivity matrix, $\{F\}$ is the vector of applied heat flows, $\{\theta_t\}$ is the vector of nodal temperatures at time t and $\{\dot{\theta}_t\}$ is the time rate of the nodal temperature values at time t. Eq.(22) was solved by the generalized trapezoidal rule. Elements with air properties were considered inside the galleries.

The considered domain was composed by the dam and a finite region of the foundation. Both were discretized with eight-node cubic elements. The dam domain of the case study was composed of 28,538 elements with 33,489 nodes and the foundation domain had 20,600 elements with 25,038 nodes. The adopted mesh is shown in Fig. 1.

2.2.3 The 1D analytical solution.

The Eq.(1) can be solved analytically under several assumptions. Given a 1D domain of width L whose extremes are located in the upstream and downstream faces and they are simultaneously subjected to harmonic temperature variations given respectively by Eq.(23) and Eq.(24), the concrete thermal field within the domain is determined by Eq.(25) (Stucky and Derron 1957).

$$\theta_u(0,t) = \overline{\theta_u} + A_{\theta,u}\, cos(\omega_\theta t) \tag{23}$$

$$\theta_d(L,t) = \overline{\theta_d} + A_{\theta,d}\, cos(\omega_\theta t) \tag{24}$$

$$\theta(L,t) = f(x)\, cos(\omega_\theta t) + \varphi(x)\, sin(\omega_\theta t) + C_5 + C_6 x \tag{25}$$

θ_u and θ_d are the concrete temperature at the upstream and downstream face respectively, $\overline{\theta_u}$ and $\overline{\theta_d}$ are the average of θ_u and θ_d, $A_{\theta,u}$ and $A_{\theta,d}$ are the amplitude of the concrete thermal wave at the upstream and downstream face and ω_θ is the frequency of the concrete thermal wave. $f(x)$, $\varphi(x)$, C_5 and C_6 are given by Eqs.(26-29).

$$f(x) = C_1\, cos(\mu x)\, cosh(\mu x) + C_2\, cos(\mu x)\, sinh(\mu x) + C_3\, sin(\mu x)\, cosh(\mu x) + C_4\, sin(\mu x)\, sinh(\mu x) \tag{26}$$

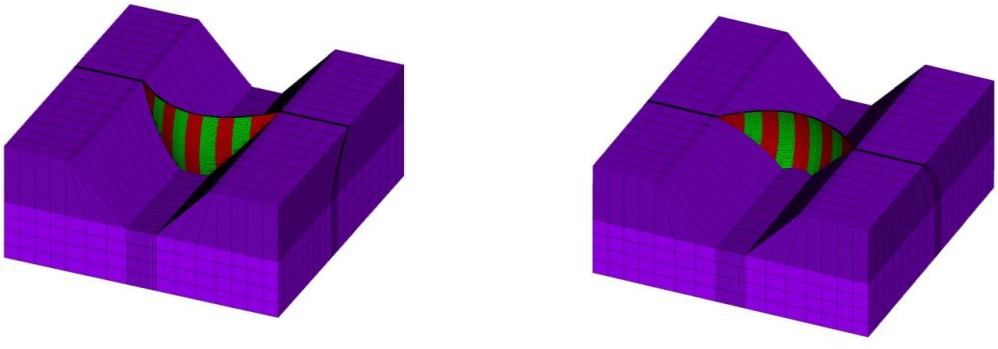

(a) (b)

Fig. 1 Adopted finite element mesh

$$\varphi(x) = -C_1\, sin(\mu x)\, sinh(\mu x) - C_2\, sin(\mu x)\, cosh(\mu x) + C_3\, cos(\mu x)\, sinh(\mu x) + C_4\, cos(\mu x)\, cosh(\mu x) \tag{27}$$

$$C_5 = \overline{\theta_u} \tag{28}$$

$$C_6 = \frac{\overline{\theta_d} - \overline{\theta_u}}{L} \tag{29}$$

where

$$C_1 = A_{\theta,u} \tag{30}$$

$$C_2 = A_{\theta,u}\, sinh(\mu L)\, \frac{\frac{A_{\theta,d}}{A_{\theta,u}} cos(\mu L) - cosh(\mu L)}{(cosh(\mu L))^2 - (cos(\mu L))^2} \tag{31}$$

$$C_3 = A_{\theta,u}\, sin(\mu L)\, \frac{\frac{A_{\theta,d}}{A_{\theta,u}} cosh(\mu L) - cos(\mu L)}{(cosh(\mu L))^2 - (cos(\mu L))^2} \tag{32}$$

$$C_4 = 0 \tag{33}$$

$$\mu = \sqrt{\frac{\omega_\theta \gamma c}{2\lambda}} \tag{34}$$

Temperatures at dam faces were decomposed into a sum of harmonic by the Fourier transformation. The solution of each harmonic was given by Eq.(25) and the final temperature was the superposition of each solution with the inverse Fourier transformation (Léger and Leclerc 2007).

This approach can deal with non-harmonic temperature variations at dam faces. However, temperatures at dam faces are not usually available. Some simplified procedures to define boundary conditions add few degrees to the air temperature to account for solar radiation and a virtual concrete thickness ΔL for convection (Léger *et al.* 1993a, 1993b). Stucky and Derron (1957) proposed Eq.(35) for computing ΔL. Temperature at dam faces under water level were imposed to be equal to water temperature in contact with them.

$$\Delta L = \frac{\lambda}{h} \tag{35}$$

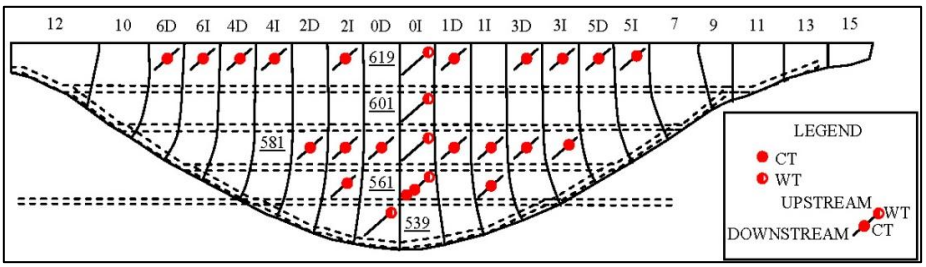

Fig. 2 The La Baells dam. Thermometers. CT=Concrete thermometer. WT= Water thermometer

2.3 Case study

The case study was the La Baells double curvature arch dam which is built on the Llobregat River in Barcelona. The dam axis direction, from upstream to downstream, is South 0º East. The maximum height is 102 m and the crest length is 403 m. Its thickness varies from 4 m at the crest to 20.1 m at the base of the central crown cantilever. Four horizontal galleries were built. Its dimensions are 1.75 m width and 2.1 m height and their bases are situated at 608.50, 589.10, 569.70 and 550.30 m above mean sea level.

There are 21 thermometers installed in the concrete and five more in the upstream face for recording water temperature. The situation of thermometers is illustrated in Fig. 2 and listed in Table 1. $V_{w,t}$, H_G, $\theta_{a,t}$, H_r, rainfall, total air pressure and water level are registered daily at the dam location. Data are available from 1 January 2006 to 31 July 2008. Material properties are listed in Table 2. Fig. 3 depicts the time series of the pool level.

Table 1 Position of thermometers. T: thickness of the dam at thermometer position. CT-619-6D: concrete thermometer situated at the 619 m above the sea level in the block 6D

Thermometer	T.(m)	Thermometer	T.(m)	Thermometer	T.(m)
CT-619-6D	6.37	CT -619-3I	6.13	CT -581-1I	13.98
CT -619-6I	6.27	CT -619-5D	6.27	CT -581-3D	14.45
CT -619-4D	6.13	CT -619-5I	6.41	CT -581-3I	15.04
CT -619-4I	6.04	CT -581-2D	13.98	CT -561-2I	16.82
CT -619-2I	5.87	CT -581-2I	13.72	CT -561-0I-2	16.51
CT -619-1D	5.87	CT -581-0D	13.55	CT -561-0I-3	16.51
CT -619-3D	6.04	CT -581-1D	13.72	CT -561-1I	17.73

Table 2 Properties of the foundation and the concrete

Material	Foundation	Concrete
Density (kg m-3)	3000	2400
Thermal conductivity (WK-1m-1)	2.20	2.43
Specific heat (JKg-1K-1)	950	982
Emissivity	0.70	0.70

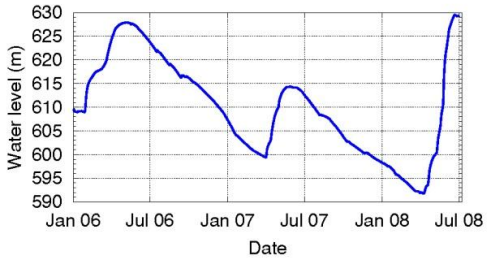

Fig. 3 Water level in the reservoir above mean sea level. Top water level is at 630.00 m above mean sea level

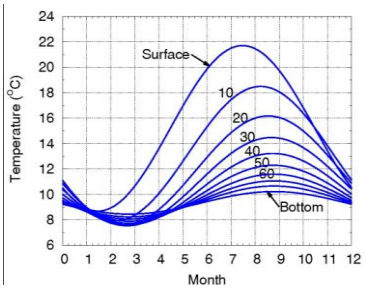

Fig. 4 Water temperature at the La Baells reservoir. Depth in meters

3. Results and discussion

3.1 The boundary conditions

3.1.1 Water temperature

Parameters of the Bofang model were estimated by the least squared method using the recorded temperatures. $\overline{\theta_{w,s}}$ is 15.19 ºC, $\overline{\theta_{w,b}}$ is 9.33 ºC, $A_{w,s}$ is 6.51 ºC and t_o is 201. Fig. 4 illustrates the evolution of the water temperature at several reservoir depths according to the model.

3.1.2 Heat fluxes

Fig. 5 shows hourly insolation on July 5, 2007 on the boundary points of three concrete thermometers: CT-619-2I in Fig. 5a, CT-581-2I in Fig. 5b and CT-581-1D in Fig. 5c. The upstream surface of the La Baells dam is north facing. Thermometers CT-619-2I and CT-581-2I are located in the same cantilever and thermometers CT-581-2I and CT-581-1D in the same arch.

Shading over the downstream face is originated by the upstream face, which prevents sunbeams from reaching some parts of the face. Insolation over these points is depicted in red dashed lines in Fig. 5. The downstream boundary point of the thermometer CT-619-2I and CT-581-2I are subjected to sunrays from 10:00 to 14:00 and the CT-581-1D from 11:00 to 16:00.

Shading over the upstream dam face is caused by the abutments and the geometry of the face, i.e., some areas of the face prevent sunrays from striking other parts of the faces. Insolation over these points is plotted in continuous blue line in Fig. 5. The boundary point of the thermometer CT-619-2I is subjected to sunrays during the whole day. Sunrays only reach the boundary point of the thermometer CT-581-2I from 16:00 to 17:00 and the thermometer CT-581-1D from 8:00 to 9:00. Shading over the boundary point of the thermometer CT-581-2I is caused by the left abutment and the upstream face from sunrise to 8:00, by the face from 9:00 to 15:00 and by the face and the right abutment from 18:00 to sunset.

Shading reduces the amount of sun energy which reaches the dam. The orientation and slope of the boundary points varies widely due to the double curvature of the faces and makes insolation to vary across them. Moreover, for a given point, insolation also varies during the day due to the atmospheric conditions and the sun position (Fig. 5).

The shading effect is highlighted by considering the downstream boundary points of the thermometers CT-581-1D and CT-581-2I. Both points are located in the same arch and their slopes and azimuths are similar. However, at 10:00 sunrays do not strike the boundary point of the thermometer CT-581-1D, while they do the other point. Insolation is, respectively, 1.3 MJ/m2 and 0.6 MJ/m2. Shading involves a 54% energy reduction.

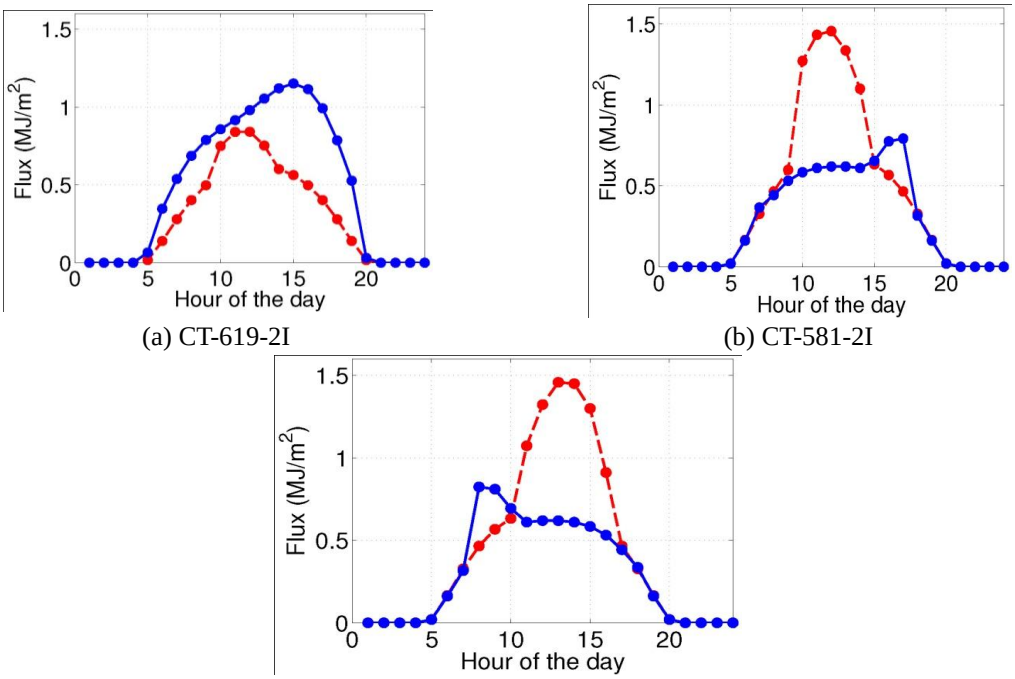

Fig. 5 Hourly insolation on July 7, 2007 on boundary points corresponding to concrete thermometers location. Red dashed lines correspond to downstream points and blue continuous lines to upstream points. Hours in local apparent time

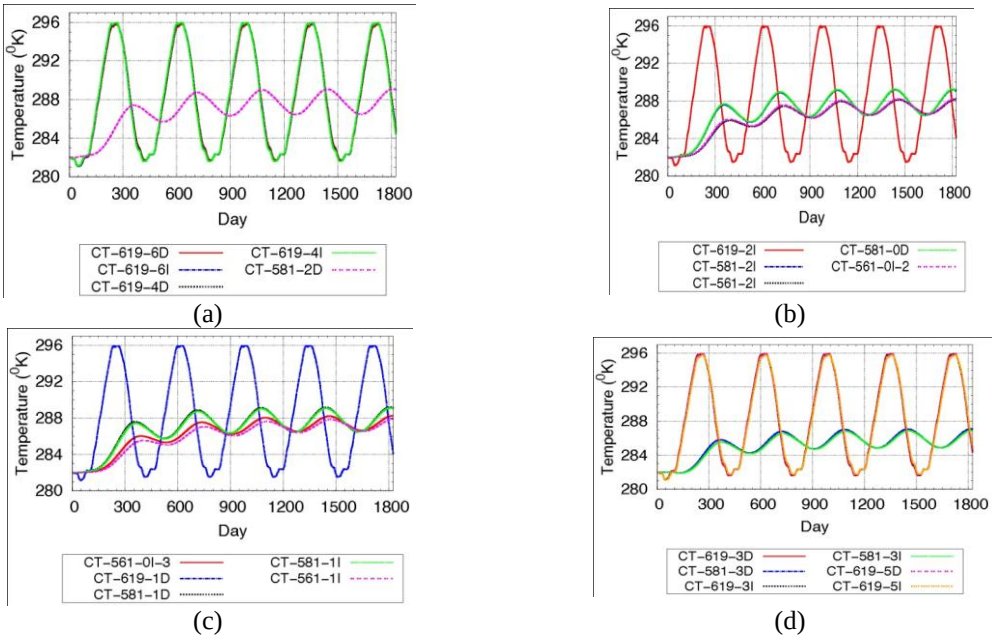

Fig. 6 Evolution of thermal state at central nodes of the integration domains computed by the improved 1D-FDS. Example: CT-619-6D: Concrete Thermometer located at height 619 meters above mean sea level in block 6D

The effects of the double curvature over the insolation are highlighted by considering the downstream boundary points of the thermometers CT-619-2I and CT-581-2I. The points have similar azimuths but different slopes and are located in the same crown cantilever. Sunrays strike both at 11:00 and insolation is 0.9 MJ/m2 and 1.5 MJ/m2 respectively. The difference is caused by the slope. The lowest point is located at the mid-height of the dam, where the face is almost vertical; while the higher, that is closer to the crest, has a negative slope. As the slope of a surface decreases, it is less likely to capture solar radiation. The same phenomenon is appreciated when insolation over the upstream boundary points at 16:00 is analyzed. In this case, the highest point has a larger slope than the lower, which is almost vertical.

3.2 Thermal model results

3.2.1 The improved and the Agullo et al. 1D-FDS models

The temperature evolution of the central nodes during the calculation of the initial thermal field are shown in Fig. 6. Convergence is reached in the fifth year. The concrete solar absortivity (0.66) was estimated by trial and error with the thermal loads of the year 2007. Finally, observations of the year 2008 were employed to evaluate the model.

The observed and predicted temperatures at the concrete thermometers are plotted in Fig. 7. Recorded data are plotted in red points and computed temperatures in blue continuous lines for the improved 1D-FDS model and in brown double dashed line for the Agullo *et al.* 1D-FDS model. The observed temperatures were estimated by the improved 1D-FDS model with a root mean squared error (RMSE) of 1.02 ºK and 1.25 ºK and a bias (B) of -0.17 ºK and -0.83 ºK, for the years 2007 and 2008 respectively. Indeed, the Agullo *et al.* 1D-FDS model provided estimates with a RMSE of 2.76 ºK and 2.19 ºK, and a B of 2.64 ºK and 2.04 ºK for the years 2007 and 2008 respectively.

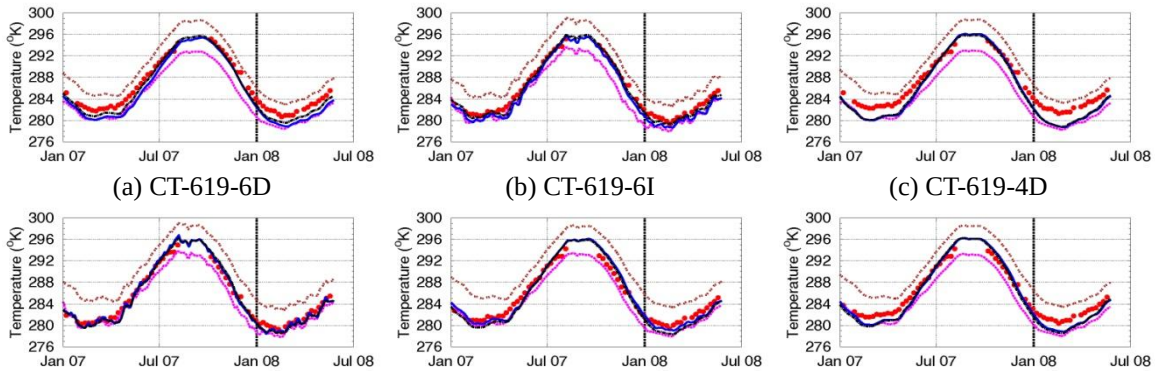

(a) CT-619-6D (b) CT-619-6I (c) CT-619-4D

(d) CT-619-4I (e) CT-619-2I (f) CT-619-1D

Fig. 7 Observed and predicted temperature at the concrete thermometers. Temperatures computed by the improved 1D-FDS model are plotted in blue continuous lines, the Agullo *et al.* 1D-FDS model in brown double dashed line, the 3D-FEM model in dash-dot black lines, the analytical solution in dashed magenta lines and observations in red points. CT-619-6D: concrete thermometer located at height 619 meters above mean sea level in block 6D

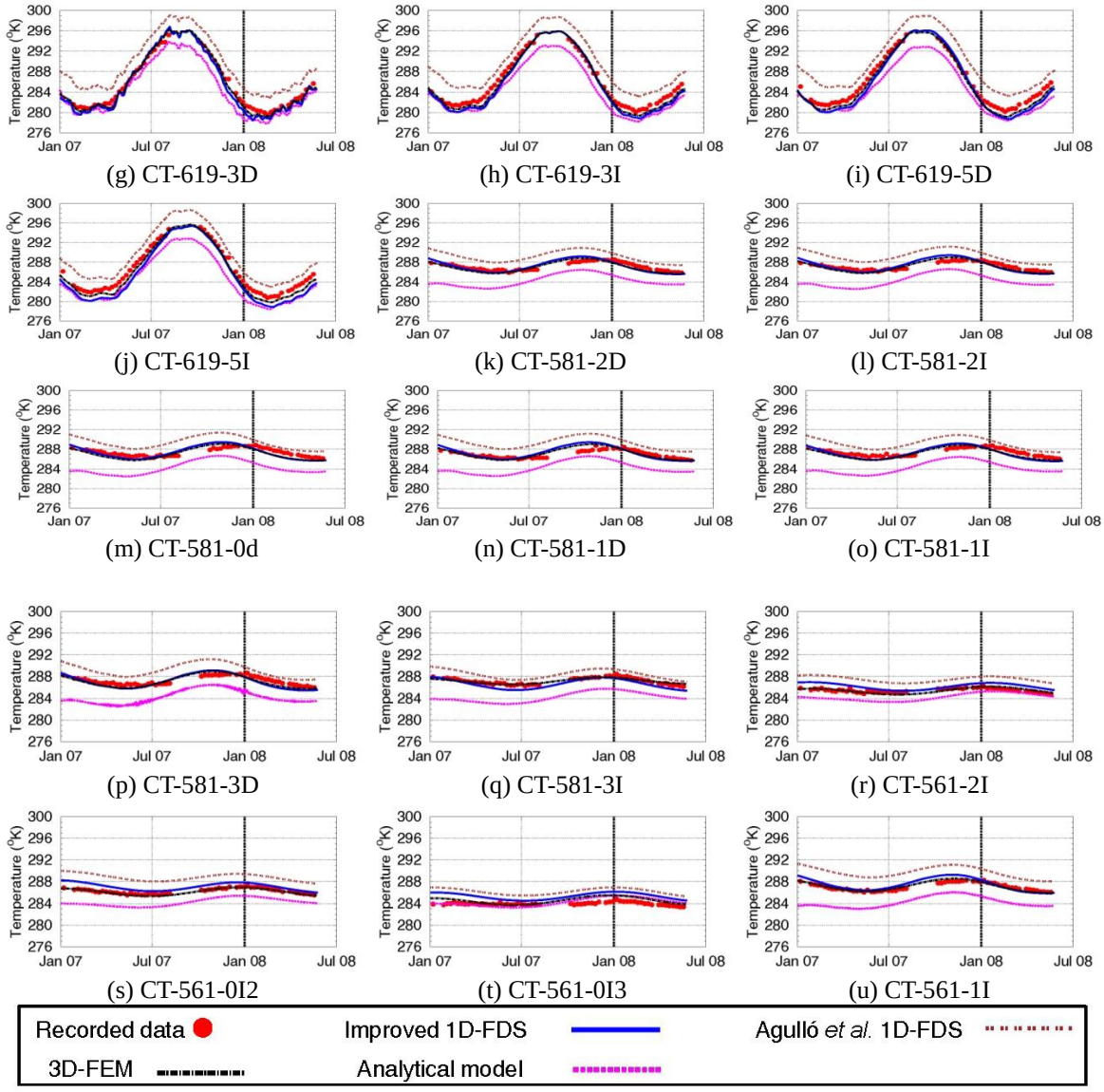

Fig. 7 Continued

3.2.2 The 3D-FEM model

Initial temperatures were determined by Eq.(25). The concrete absortivity was 0.66. The computed temperatures at the thermometers are depicted in Fig. 7 in dash-dot black lines. The observed temperatures were estimated with a RMSE of 0.75 ºK and 0.98 ºK, and a B of -0.25 ºK and -0.70 ºK, for the years 2007 and 2008 respectively.

3.2.3 The analytical solution

Air temperature was used as a boundary condition in the extremes of the domain in contact with air, since concrete temperatures at dam face are unknown. Extremes in contact with water

were supposed to have the same temperature as the fluid. The virtual concrete thickness was computed through Eq.(35). A mean value equal to 0.15 m was added to account for convection and solar radiation was not considered.

The predicted temperatures at the thermometers locations are plotted in Fig. 7 in dashed magenta lines. The observed temperatures were estimated with a RMSE of 2.79 ºK and 2.51 ºK, and a B of -2.55 ºK and -2.38 ºK, for the years 2007 and 2008 respectively.

3.2.4 Comparison between models and attributions

The average model performance was assessed by the statistics root mean squared error and bias. Results are listed in Table 3. As can be observed, the numerical models provide, in general, predictions that are more approximated to the observed temperatures, because they took fewer simplifications. Among the numerical models a significant difference is also detected between the Agullo *et al.* 1D-FDS model and the and the improved 1D-FDS and the 3D-FEM models. This difference is also derived from the number of simplifications taken, as the methodology to compute heat fluxes for both the improved 1D-FDS and the 3D-FEM models considered a larger number of the involved physical phenomena.

The analytical solution provided predictions with significant errors due to the adopted simplifications. The main source of errors comes from the imposed boundary condition at nodes incontact with air. Its temperature was assumed to be equal to air temperature while solar radiation and evaporative cooling were not taken into account. For that reason, the computed temperatures are often lower than the observations, with negative values of the bias (Table 3). The performance of the analytical model is poorer than that of the improved 1D-FDS model. The RMSE is more than twice and the bias is more than three times for the years 2007 and 2008 (Table 3).

A large difference is detected when the Agullo *et al.* 1D-FDS and the improved 1D-FDS models are compared. The new methodology for computing boundary conditions improves considerably the results of the Agullo *et al.* model. RMSE is reduced by 63 % and 43 % for the years 2007 and 2008 respectively. The Agullo *et al.* model provides higher temperatures than observed ones, since some heat transfer mechanisms which cool the dam are not considered. Estimates are up to 2.5 ºK higher than observations, as it can be appreciated in Fig. 7. Instead, the proposed approach leads to a bias lower than 1.0 ºK.

Results of the improved 1D-FDS model and the 3D-FEM model are very similar, except in the vicinity of the abutments. This attribution can be explained when heat fluxes through the dam are analyzed, as the integration domain in the improved 1D-FDS model is a line and, consequently, lateral fluxes are neglected. By contrast, heat diffuses into all directions in the 3D-FEM model.

Fig. 8 depicts the thermal flux through the central crown cantilever on July 7, 2007 (Fig. 8a) and on November 17, 2007 (Fig. 8b), and through the left abutment of arch at z=8 m on November 17, 2007 (Fig. 6c).

On July 7, 2007 the ambient temperature was 292.3 ºK and solar radiation was striking the dam. Both factors generated a positive heat flux which heated the concrete. By contrast, an outflow is presented on November 17, 2007. Air temperature was approximately 283.2 ºK for the previous 45 days. A sudden drop occurred on November 17, 2007, when air temperature was -273.1 ºK. This produced an outflow heat flow.

The fluxes through the crown cantilevers and the arch approximately follow a normal direction to dam faces. However, the flow is affected by the presence of the foundation which changes the direction of the heat propagation, especially in the abutments.

Table 3 Performance of the thermal models

Model	RMSE (ºK)		B (ºK)	
	2007	2008	2007	2008
Analytical	2.79	2.51	-2.55	-2.38
Agullo *et al.* 1D-FDS	2.76	2.19	2.64	2.04
Improved 1D-FDS	1.02	1.25	-0.17	-0.83
3D-FEM	0.75	0.98	-0.25	-0.70

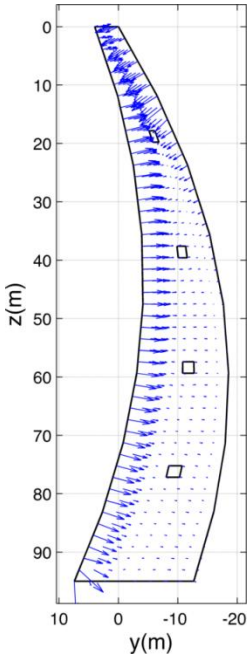

(a) Central crown cantilever on July 5, 2007

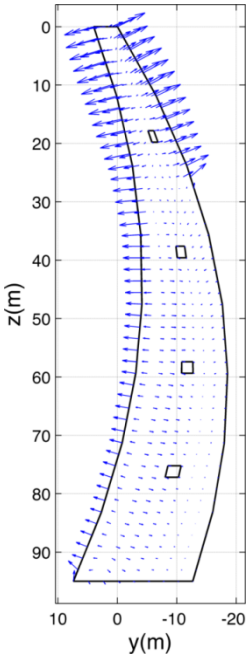

(b) Central crown cantilever on November 17, 2007

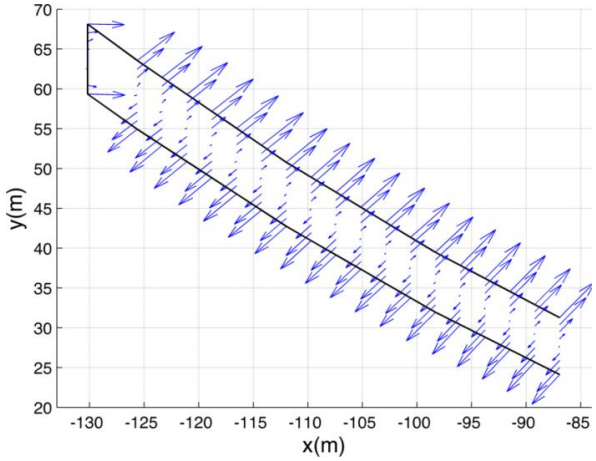

(c) Left abutment of arch at z=8 m on November 17, 2007

Fig. 8 Thermal flux computed by the 3D numerical model. The magnitude of the flux is proportional to the length of the arrows

The thermometers installed in La Baells dam are located in arch at equal intervals from the galleries. Since the domain considered in the improved 1D-FDS model is normal to the mid-dam surface, its direction is similar to the heat flux ones in those areas. This leads to more accurate estimates of temperatures.

The thermal field of the two above mentioned parts of the dam for the years 2007 and 2008 were computed by the three considered numerical models. The mean absolute difference (MAE) between the results of the improved 1D-FDS and the 3D-FEM models is depicted in Fig. 9a and 9b and between the Agullo *et al.* 1D-FDS and the 3D-FEM models in Fig. 9c and 9d.

The difference between the improved 1D-FDS and the 3D-FEM models is on average lower than 0.7 ºK in most parts of the dam, except in the vicinity of the foundation due to the direction of the fluxes in that area (Fig. 9a and 9b). Moreover, the analysis of the bias (not depicted) shows that the 1D model provides in general higher temperatures than the 3D model.

On another note, the mean difference between the Agullo *et al.* 1D-FDS and the 3D-FEM models is, on average, 2.8 ºK (Fig. 9c and 9d). The 1D model provided higher temperatures than the 3D model, since the cooling heat transfer mechanisms and shades were ignored.

The largest values of MAE in Fig. 9c are located in the areas close to the sun-exposed faces: the downstream face and the upper third of the upstream face, where a boundary condition of imposed heat flux was employed. The difference decreases as the considered point is closer to the mid-face, since atmospheric effects are substantially dampened by the concrete thickness. The downstream surface is south facing and, consequently, exposed to sun rays. However, the abutments and the crest of the dam shade some areas of the face along the day and, as a result, the solar energy reaching the dam is undermined. A similar phenomenon occurs in the upper third of the upstream face. This surface is north facing and, therefore, most of the time is in the shade, a fact that was not considered under the Agullo *et al.* 1D-FDS model. Moreover, night and evaporative cooling were not accounted for.

The upper third of the upstream face (panel 9c and 9d) has larger values of MAE than the downstream face. Both areas were above water level and, consequently, exposed to sun rays for the years 2007 and 2008. The downstream face of the real dam receives more energy from the sun than the upstream since the latter is north facing and it is shaded most of the time. Shading reduce the amount of solar energy reaching the surfaces, but it was not accounted for in the numerical model. The consequence is larger error in the north facing areas than in the south facing.

The difference between models is nearby zero in the lower two-thirds of the upstream face. This area was under water level most of the time and, consequently, the temperature of the boundary nodes was imposed to be equal to water temperature. This condition was employed in all models and the water temperature was computed though the same approach.

Galleries were considered by using air nodes or elements inside them. Fig. 10a shows a zoom of Fig 9a in the area of the highest gallery. Another way to model the galleries is by imposing a heat flux between its surface and the air within them (Fig. 10b). However, air temperature and speed have to be known. The thermal field of the crown cantilever was also computed by the improved 1D-FDS and the 3D-FEM models where a thermal flux was imposed in the contours of the galleries. Air within galleries was assumed to be 283.2 ºK and still. The mean absolute difference between concrete temperatures computed by the models in the area of the highest gallery is depicted in Fig. 10b. By comparing Fig 10a and Fig. 10b, a large difference is found in the last model. As a result, speed and temperature of air inside the galleries should be monitored and different ways to model the thermal behavior of galleries lead to substantial differences between results.

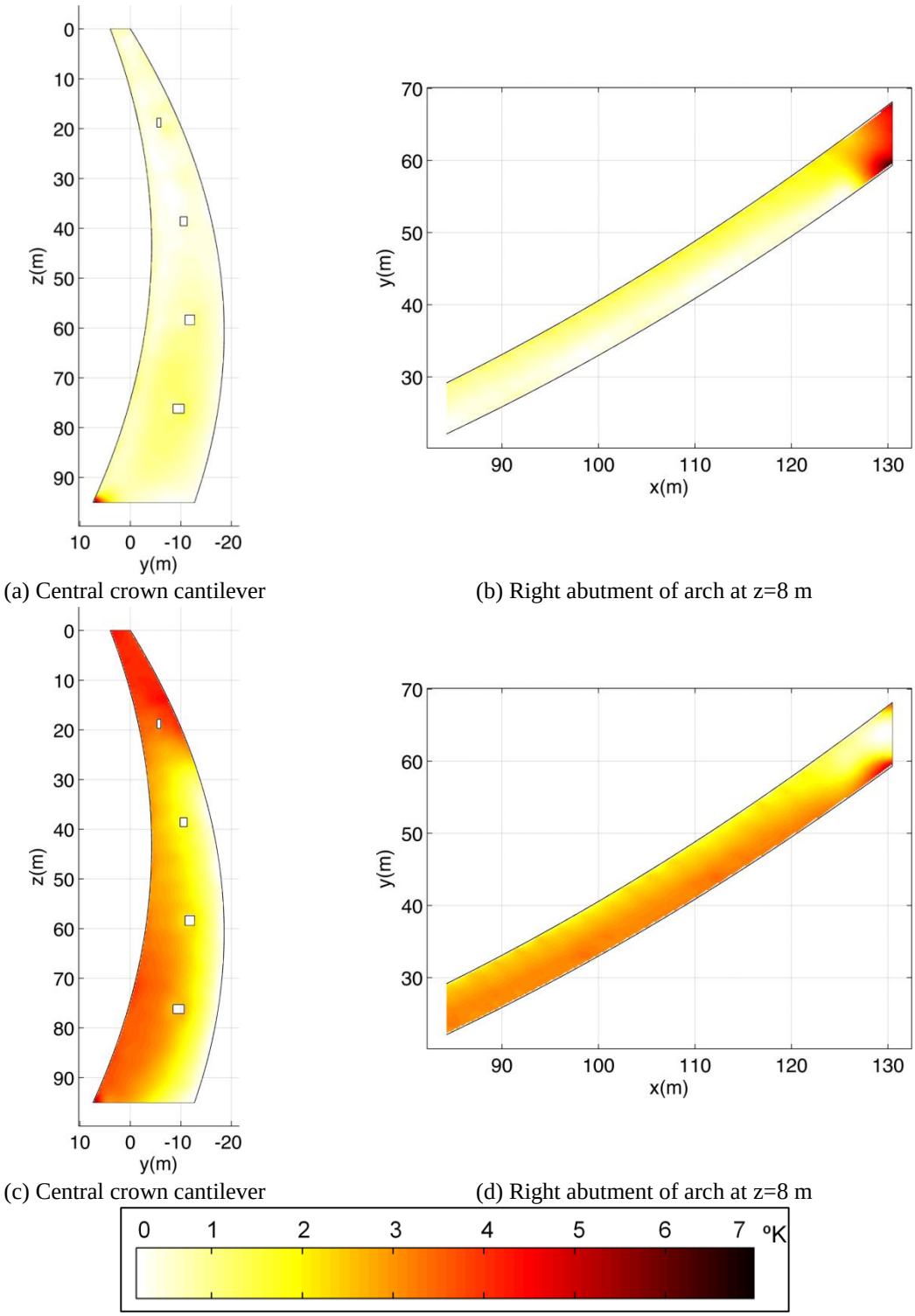

(a) Central crown cantilever (b) Right abutment of arch at z=8 m

(c) Central crown cantilever (d) Right abutment of arch at z=8 m

Fig. 9 Mean absolute difference between the computed thermal field by the (a)-(b) improved 1D-FDS and 3D-FEM models and by (c)-(d) Agullo *et al.* 1D-FDS and 3D-FEM models

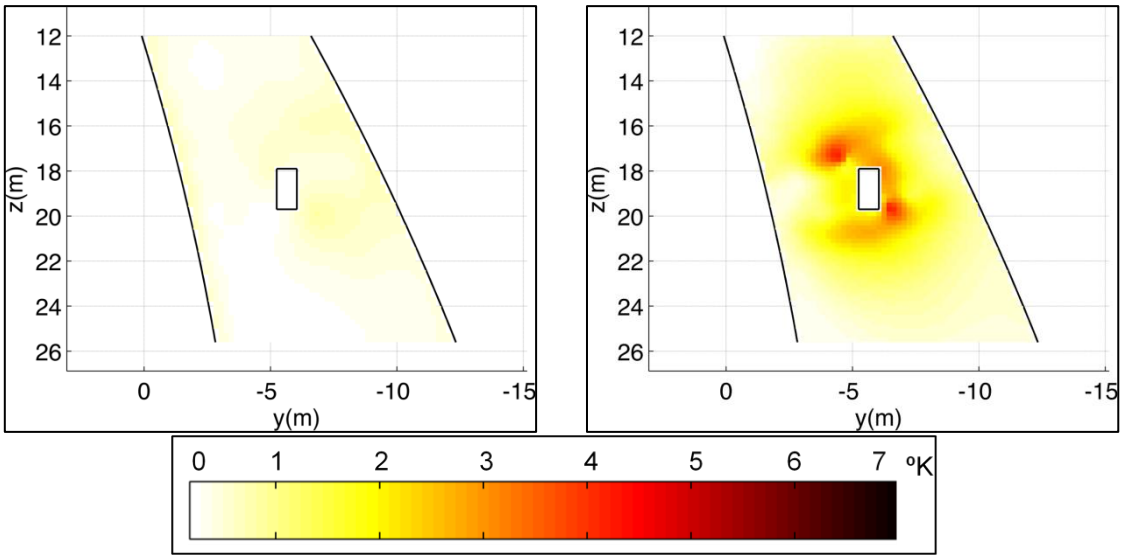

(a) Air nodes in galleries (b) Imposed heat flux in galleries

Fig. 10 Mean absolute difference between the computed thermal field by the improved 1D-FDS model and by the 3D-FEM model. Zoom of the highest gallery

Table 4 Contribution of heat transfer mechanism to model accuracy

Improved 1D-FDS model	RMSE (ºK)		B (ºK)	
	2007	2008	2007	2008
Original	1.02	1.25	-0.17	-0.83
Without solar radiation	4.48	4.73	-4.28	-4.54
Without night and evaporative cooling	2.25	1.70	2.13	1.55
Without night and evaporative cooling and shades	2.76	2.19	2.64	2.04

The contribution of the solar radiation to model accuracy was assessed by estimating the recorded temperatures at the thermometers with a 1D-FDS model whose boundary conditions were calculated without solar radiation. Results are listed in Table 4. RMSE and bias increase by more than four times when solar radiation is not considered. Moreover, computed temperatures were lower than observations.

A similar experiment was conducted with the cooling heat transfer mechanisms: night and evaporative cooling. Results are included in Table 4. RMSE and bias raise approximately twice when cooling mechanisms are ignored and computed temperatures are higher than observations. Moreover, estimates are poorer when shading is also ignored. RMSE and bias increase further, since more solar energy reaches the dam faces.

4. Conclusions

The one dimensional finite (1D) numerical approach based on a explicit finite difference scheme (FDS) model proposed by Agullo *et al.* (1996) has been improved by the use of a new methodology for computing heat fluxes developed by Santillán *et al.* (2014). This new

methodology takes into account physical phenomena which were previously unconsidered, such as: the evaporative and night radiating cooling and shading. This new model is denoted as improved 1D-FDS model.

The performance of the new approach for computing the temperature field of concrete dams has been assessed through the case study of the La Baells arch dam. Besides, the proposed model has also been compared with the original Agullo *et al.* 1D-FDS model, the classical analytical solution of Stucky and Derron (1957) and a complete three-dimensional (3D) numerical model solved by the finite element method (FEM).

The boundary conditions of the improved 1D-FDS and the 3D-FEM models were computed through the cited Santillán *et al.* (2014) methodology; which takes into account air temperature, water temperature, wind speed, solar radiation, night cooling, evaporative cooling and shading. A heat flux was imposed in the boundaries where concrete was in contact with air and a temperature equal to water temperature where the concrete was in contact with water.

Recorded concrete temperatures at the case study were estimated by the above mentioned models. The poorest estimations were provided by the 1D analytical solution. The numerical models provided similar results when boundary conditions were computed though the Santillán *et al.* (2014) methodology. The improved 1D-FDS model led to more accurate predictions than the Agullo *et al.* 1D-FDS model. The root mean squared error was reduced up to a 57 % in the case study.

The 1D analytical model provided poorer estimations than the others since solar radiation was not taken into account, among other simplifications. Consequently, temperature predictions are more similar to observations as boundary conditions does.

The improved 1D-FDS model had a linear integration domain whose direction was normal to the mid-surface of the dam. The 3D model showed that heat mainly flows in that direction, except in the vicinity of the foundation. The thermal field of the central crown cantilever and an arch were computed by the 3D-FEM and the improved 1D-FDS models. Results showed that the 1D model was as accurate as the 3D model, except in the vicinity of the abutments.

The contribution of the solar radiation, night and evaporative cooling and shading to improve the accuracy was analyzed in the case study. Solar radiation was the most influential factor, errors increased by more than four times when was ignored. The night and evaporative cooling and shades were also important factors. Errors increased approximately by twice when these phenomena were not considered.

The 1D-FDS model is computationally straightforward. Moreover, FDS models can be easily implemented in contrast to FEM models. Also, results of both models are very similar, except in the areas closed to the abutments.

The ease of implementation of the 1D-FDS model and its computational effectiveness makes it an efficient tool for practitioners and researches. Moreover, accurate results have been obtained when applied to arch and gravity dams (Agullo *et al.* 1996). However, certain parameters need to be calibrated and, consequently, observed temperatures are needed. During the design phase of dams, recorded data are not available. In such cases, the thermal field may be computed though probabilistic approaches, i.e., by considering unknown parameters as probabilistic variables whose values vary inside a defined range, and computing several thermal fields which included a representative variety of values of the parameters.

As external temperature variations cause the second most major repairs in dams during service, thermal studies are vital during the design and monitoring phases of infrastructures. The reported

methodology can be easily extended to other regions of the world. Moreover, it provides a useful tool for computing thermal stresses and it can also be used in other civil infrastructures, such as bridges.

Acknowledgments

This work was supported by the Ministerio de Economía y Competitividad (Spanish Ministry of Economy and Competitiveness) under code IPT-2012-0813-390000, titled "Desarrollo del Software iCOMPLEX para el control y evaluación de la seguridad de infraestructuras críticas" (Development of the iCOMPLEX software for the control and assessment of the safety of critical infrastructures).

The authors also thank the company Ofiteco and l'Agència Catalana de l'Aigua (the Catalan Water Agency) for recorded data from the La Baells Dam.

Abbreviations

B	Bias
D	Dimension
FDS	Finite difference scheme
FEM	Finite element method
MAE	Mean absolute error
RMSE	Root mean squared error

Notation

A	Anisotropy index
$A_{\theta,d}$	Amplitude of the concrete thermal wave at the downstream face
$A_{\theta,u}$	Amplitude of the concrete thermal wave at the upstream face
$A_{w,s}$	Annual water temperature amplitude at the surface
a	Solar absorptivity
C	Specific heat matrix
C_s	Stefan-Boltzmann constant
c	Specific heat
c_s	Specific heat capacity of air
d	Day of the year
d_o	Day at which ambient temperature is maximum
E_s	Moisture emissivity coefficient
e	Emissivity
e_s	Saturation vapour pressure
F	Vector of applied heat flows
g_r	Ground reflectivity
H	Depth of reservoir

H_G	Daily global insolation on a horizontal surface
$H_{G,o}$	Extraterrestrial daily global insolation on a horizontal surface
H_r	Relative humidity
h	Convection coefficient
h_w	Latent heat of evaporative water
I_G	Hourly global insolation on a horizontal surface
$I_{G,o}$	Extraterrestrial hourly global insolation on a horizontal surface
$I_{T,G}$	Hourly global insolation on a tilted surface
$I_{T,b}$	Hourly beam insolation on a tilted surface
$I_{T,d}$	Hourly diffuse insolation on a tilted surface
$I_{T,d,cs}$	Hourly circumsolar diffuse insolation on a tilted surface
$I_{T,d,hb}$	Hourly horizon brightening diffuse insolation on a tilted surface
$I_{T,d,iso}$	Hourly isotropic diffuse insolation on a tilted surface
$I_{T,r}$	Hourly reflected insolation on a tilted surface
I_b	Hourly beam insolation on a horizontal surface
I_d	Hourly diffuse insolation on a horizontal surface
K	Conductivity matrix
K_t	Daily global clearness index
k_t	Hourly global clearness index
k_d	Hourly diffuse fraction
L	Width
P	Total air pressure
q	Heat flux
q_c	Heat flux due to convection
q_{ev}	Heat flux due to water evaporation
q_m	Moisture evaporative flux
q_r	Heat flux due to long wave radiation exchange
q_s	Heat flux due to solar radiation
R_b	Ratio of beam insolation on a tilted surface to that on a horizontal surface
r_o	Ratio of extraterrestrial hourly global insolation to extraterrestrial daily global insolation
r_t	Ratio of hourly global insolation to daily global insolation
S_o	Day length
t	Time
V_w	Wind speed
z	Vertical distance between the dam crest and the water surface of the reservoir
α_o	Extraterrestrial daily-average solar elevation angle
β	Slope of surface
δ	Solar declination angle
θ_t	Vector of nodal temperatures at time t
θ	Concrete temperature
θ_a	Air temperature
θ_d	Concrete temperature at downstream face
θ_{dp}	Dew point temperature

$\overline{\theta_d}$	Average concrete temperature at the downstream face
θ_{sk}	Sky temperature
θ_u	Concrete temperature at upstream face
$\overline{\theta_u}$	Average concrete temperature at the upstream face
θ_w	Water temperature
$\overline{\theta_{w,b}}$	Mean annual water temperature at the bottom of the reservoir
$\overline{\theta_{w,s}}$	Mean annual water temperature at the surface of the reservoir
λ	Thermal conductivity
ρ	Density
ϕ	Latitude
ω	Solar hour angle
ω_o	Sunrise hour angle
ω_w	Angular frequency of the water temperature
ω_θ	Frequency of the concrete thermal wave
Δx	Mesh size
Δt	Step time

References

Abdulrazeg, A.A., Noorzaei, J., Mohammed, T.A. and Jaafar, M.S. (2013), "Modeling of combined thermal and mechanical action in roller compacted concrete dam by three-dimensional finite element method", *Struct. Eng. Mech.*, **47**(1), 1-25.

Abdulrazeg, A.A., Noorzaei, J., Jaafar, M.S., Khanehzaei, P. and Mohamed, T.A. (2014), "Thermal and structural analysis of RCC double-curvature arch dam", *J. Civ. Eng. Manag.*, **20**(3), 434-445.

Agullo, L., Mirambell, E. and Aguado, A. (1996), "A model for the analysis of concrete dams due to environmental thermal effects", *Int. J. Numer. Methods Heat Fluid Flow*, **6**(4), 25-36.

Bayagoob, K.H., Noorzaei, J., Abdulrazeg, A.A., Al-Kami, A.A. and Jaafar, M.S (2010), "Coupled thermal and structural analysis of roller compacted concrete arch-dam by three-dimensional finite element method", *Struct. Eng. Mech.*, **36**(4), 401-419.

Bentz, D.P. (2000). *A computer model to predict the surface temperature and time-of-wetness of concrete pavements and bridge decks*. US Department of Commerce, NISTIR 6551, available at http://ciks.cbt.nist.gov/bentz/nistir6551/tpredict.html.

Bofang, Z. (1997), "Prediction water temperature in deep reservoirs", *Dam Engineering*, **8**(1), 13-25.

Chen, B., Clark, D., Maloney, J., Mei, W. and Kasher, J. (1995), "Measurement of night sky emissivity in determining radiant cooling from cool storage roofs and roof ponds", In *Proceedings of the National Passive Solar Conference*, Vol. 20, pp. 310-313. American Solar Energy Society Inc.

Chuntranuluck, S., Wells, C.M. and Cleland, A.C. (1998), "Prediction of chilling times of foods in situations where evaporative cooling is significant-part 1. method development", *J. Food Eng.*, **37**(2), 111-125.

De Miguel, A., Bilbao, J., Aguiar, R. Kambezidis, H. and Negro, E. (2001), "Diffuse solar irradiation model evaluation in the north Mediterranean belt area", *Sol. Energy*, **70**(2), 143-53.

Diez-Mediavilla, M., De Miguel, A. and. Bilbao, J. (2005), "Measurement and comparison of diffuse solar irradiance models on inclined surfaces in Valladolid (Spain)", *Energy Conv. Manag.*, **46**(13), 2075-2092.

Douglas, K.J. (2002), "The shear strength of rock masses", Ph.D. Dissertation, The University of New South Wales, Sydney, NSW, Australia.

Duffie, J.A. and Beckman, W.A. (2013), *Solar Engineering of Thermal Processes*, 4th ed., John Wiley & Sons, Inc, Hoboken, NJ, USA.

Elminir, H.K. (2007), "Experimental and theoretical investigation of diffuse solar radiation: Data and models quality tested for Egyptian sites", *Energy*, **32**, 73-82.
Faria, R., Azenha, M. and Figueiras, J.A. (2006), "Modelling of concrete at early ages: application to an externally restrained slab", *Cem. Concr. Comp.*, **28**, 572-585.
Gueymard, C. (2000), "Prediction and performance assessment of mean hourly global radiation", *Sol. Energy*, **68**(3), 285-303.
Incropera, F.P., Lavine, A.S. and. De Witt, D.P. (2011), *Fundamentals of Heat and Mass Transfer*, 7th ed., John Wiley & Sons Incorporated, USA.
Jacovides, C.P., Tymvios, F.S., Assimakopoulos, V.D. and Kaltsounides, N.A. (2006), "Comparative study of various correlations in estimating hourly diffuse fraction of global solar radiation", *Renew. Energy*, **31**, 2492-2504.
Jamil Ahmad, M. and Tiwari, G.N. (2008), "Study of models for predicting the mean hourly global radiation from daily summations", *Open Environmental Sciences*, **2**, 6-14.
Jin, F., Chen, Z., Wang, J. and Yang, J. (2010), "Practical procedure for predicting non-uniform temperature on the exposed face of arch dams", *Appl. Therm. Eng.*, **30**(14), 2146-2156.
Kim, S.H., Cho, K.I., Won, J.H. and Kim, J.H. (2009), "A study on thermal behaviour of curved steel box girder bridges considering solar radiation", *Arch. Civ. Mech. Eng*. **9**(13), 59-76.
Léger, P. and Leclerc, M. (2007), "Hydrostatic, temperature, time-displacement model for concrete dams", *J. Eng. Mech.*, **133**(3), 267-277.
Léger, P., Venturelli, J. and Bhattacharjee, S.S. (1993a), "Seasonal temperature and stress distributions in concrete gravity dams. Part I: Modelling", *Can. J. Civ. Eng.*, **20**(6), 999-1017.
Léger, P., Venturelli, J. and Bhattacharjee, S.S. (1993b), "Seasonal temperature and stress distributions in concrete gravity dams. Part II: Behaviour", *Can. J. Civ. Eng.*, **20**(6), 1018-1029.
Mata, J. (2011), "Interpretation of concrete dam behaviour with artificial neural network and multiple linear regression models", *Eng. Struct*., **33**(3), 903-910.
Mata, J., Tavares de Castro, A. and Sá da Costa, J. (2013), "Time–frequency analysis for concrete dam safety control: Correlation between the daily variation of structural response and air temperature", *Eng. Struct*., **48**, 658-665.
Malm, R. and Ansell, A. (2011), "Cracking of concrete buttress dam due to seasonal temperature variation", *ACI Struct. J.*, **108**(1), 13-22.
Mirambell, E. and Aguado, A. (1990), "Temperature and stress distributions in concrete box girder bridges", *J. Struct. Eng.*, **116**(9), 2388-2409.
Nejad, F.M., Ghafari, S. and Afandizadeh, S. (2013), "Numerical analysis of thermal and composite stresses in prestressed concrete pavements", *Comput. Concrete*, **11**(2), 169-182.
Noorian, A., Moradi, I., and Kamali, G. (2008), "Evaluation of 12 models to estimate hourly diffuse irradiation on inclined surfaces", *Renew. Energy*, **33**(6), 1406-1412.
Notton, G., Poggi, P. and Cristofari, C. (2006), "Predicting hourly solar irradiations on inclined surfaces based on the horizontal measurements: Performances of the association of well-known mathematical models", *Energy Conv. Manag.*, **47**, 1816-1829.
Oliveira, A.P., Escobedo, J.F., Machado, A.J., Soares, J. (2002), "Correlation models of diffuse solar radiation applied to the city of Sao Paulo, Brazil", *Appl. Energy*, **71**, 59-73.
Reindl, D.T, Beckman, W.A. and Duffie, J.A. (1990), "Evaluation of hourly tilted surface radiation models", *Sol. Energy*, **45**(1), 9-17.
Santillán, D., Salete, E., Vicente, D. and Toledo, M. (2014), "Treatment of solar radiation by spatial and temporal discretization for modeling the thermal response of arch dams", *J. Eng. Mech.*, **140**(11), 05014001.
Sheibany, F. and Ghaemian, M. (2006), "Effects of environmental action on thermal stress analysis of Karaj concrete arch dam", *J. Eng. Mech.*, **132**(5), 532-544.
Soares, J., Oliveira, A.P., Boznar, M.Z., Mlakar, P., Escobedo, J.F., Machado, A.J. (2004), "Modeling hourly diffuse solar radiation in the city of Sao Paulo using a neural-network technique", *Appl. Energy*, **79**, 201-214.

Stucky, A. and Derron, M.H. (1957), *Problèmes Thermiques Posés par la Construction des Barrages-rèservoirs*, P. Feissly, ed., Science & Technique, Lausanne, Switzerland.
Tham, Y., Muneer, T. and Davison, B. (2010), "Estimation of hourly averaged solar irradiation: evaluation of models", *Building Services Engineering Research and Technology*, **31**(1), 9-25.
Vartiainen, E. (2000), "A new approach to estimating the diffuse irradiance on inclined surfaces", *Renew. Energy*, **20**(1), 45-64.
Wojcik, G.S., Fitzjarrald, D.R. and Plawsky, J.L. (2003), "Modelling the interaction between the atmosphere and curing concrete bridge decks with the SLABS model", *Meteorol. Appl.*, **10**(2), 165-186.

CC